An integrated technique for rapid gas permeability measurement of tight rock media

Tao Zhang[1], Qinhong Hu[1,2*], Behzad Ghanbarian[3], Derek Elsworth[4], Zhiming Lu[5]

[1] Department of Earth and Environment Sciences, University of Texas at Arlington, Arlington, TX 76019, United States

[2]National Key Laboratory of Deep Oil and Gas, China University of Petroleum (East China), Qingdao 266580, P.R. China

[3] Porous Media Research Lab, Department of Geology, Kansas State University, Manhattan, KS 66506, United States

[4] Department of Energy and Mineral Engineering, G3 Centre and Energy Institute, The Pennsylvania State University, University Park, PA 16802, United States

[5] The Earth and Environmental Sciences Division, Los Alamos National Laboratory, Los Alamos, NM 87544, United States

Prepared for

Hydrology and Earth System Sciences

August 26, 2023

* Corresponding author: huqinhong@upc.edu.cn

Abstract: Nano-darcy level permeability measurements of porous media, such as nano-porous mudrocks, are frequently conducted with gas invasion methods into granular-sized samples with short diffusion lengths and thereby reduced experimental duration; however, these methods lack rigorous solutions and standardized experimental procedures. For the first time, we resolve this by providing an integrated technique (termed as gas permeability technique) with coupled theoretical development, experimental procedures, and data interpretation workflow. Three exact mathematical solutions for transient and slightly compressible spherical flow, along with their asymptotic solutions, are developed for early- and late-time responses. Critically, one late-time solution is for an ultra-small gas-invadable volume, important for a wide range of practical usages. Developed as applicable to different sample characteristics (permeability, porosity, and mass) in relation to the storage capacity of experimental systems, these three solutions are evaluated from essential considerations of error difference between exact and approximate solutions, optimal experimental conditions, and experimental demonstration of mudrocks and molecular-sieve samples. Moreover, a practical workflow of solution selection and data reduction to determine permeability is presented by considering samples with different permeability and porosity under various granular sizes. Overall, this work establishes a rigorous, theory-based, rapid,

and versatile gas permeability measurement technique for tight media at sub-nano darcy levels.

Keywords: permeability; granular samples; pulse-decay; mathematical solutions; experimental methods.

Highlights:

- An integrated (both theory and experiments) gas permeability technique (GPT) is presented.
- Exact and approximate solutions for three cases are developed with error discussion.
- Conditions of each mathematical solution are highlighted for critical parameters.
- Essential experimental methodologies and data processing procedures are provided and evaluated.

1. Introduction

Shales, crystalline, and salt rocks with low permeabilities (e.g., $<10^{-17}$ m^2 or 10 micro-darcies μD) are critical components to numerous subsurface studies. Notable examples are the remediation of contaminated sites(Neuzil, 1986; Yang et al., 2015), long-term performance of high-level nuclear waste repositories (Kim et al., 2011; Neuzil, 2013), enhanced geothermal systems (Huenges, 2016; Zhang et al., 2021), efficient development of unconventional oil and gas resources (Hu et al., 2015; Javadpour, 2009), long-term sealing for carbon utilization and storage (Fakher et al., 2020; Khosrokhavar, 2016), and high-volume and effective gas (hydrogen) storage (Liu et al., 2015; Tarkowski, 2019). For fractured rocks, the accurate characterization of rock matrix and its permeability is also critical for evaluating the effectiveness of low-permeability media, particularly when transport is dominated by slow processes like diffusion (Ghanbarian et al., 2016; Hu et al., 2012).

Standard permeability test procedures in both steady-state and pulse-decay methods use consolidated cm-sized core-plug samples, which may contain fractures and show dual- or triple-porosity characteristics (Abdassah and Ershaghi, 1986; Bibby, 1981). The overall permeability may therefore be controlled by a few bedding-oriented or cross-cutting fractures, even if experiments are conducted at reservoir pressures (Bock et al., 2010;

75 Gensterblum et al., 2015; Gutierrez et al., 2000; Luffel et al., 1993). Fractures
76 might be naturally- or artificially-induced (e.g., created during sample
77 processing), which makes a comparison of permeability results among
78 different samples difficult (Bock et al., 2010; Gensterblum et al., 2015;
79 Gutierrez et al., 2000; Luffel et al., 1993). Hence, methods for measuring the
80 matrix (non-fractured) permeability in tight media, with a practical necessity
81 of using granular samples, have attracted much attention to eliminate the sides
82 effect of fractures (Civan et al., 2013; Egermann et al., 2005; Heller et al.,
83 2014; Wu et al., 2020; Zhang et al., 2020).

84 A GRI (Gas Research Institute) method was developed by Luffel et al. (1993)
85 and followed by Guidry et al. (1996) to measure the matrix permeability of
86 crushed mudrocks (Guidry et al., 1996; Luffel et al., 1993). Such a method
87 makes permeability measurement feasible in tight and ultra-tight rocks (with
88 permeability $< 10^{-20}$ m^2 or 10 nano-dcarcies, nD), particularly when
89 permeability is close to the detection limit of the pulse-decay approach on core
90 plugs at ~10 nD (e.g., using commercial instrument of PoroPDP-200 of
91 CoreLab). In the GRI method, helium may be used as the testing fluid to
92 determine permeability on crushed samples at different sample sizes (e.g.,
93 within the 10-60 mesh range, which is from 0.67 mm to 2.03 mm). The limited
94 mesh size of 20-35 (500-841 μm in diameter) was recommended in earlier

works, which has led to the colloquial names of "the GRI method/size" in the literature (Cui et al., 2009; Kim et al., 2015; Peng and Loucks, 2016; Profice et al., 2012). However, Luffel et al. (Guidry et al., 1996; Luffel et al., 1993) did not document the processing methodologies needed to derive the permeability from experimental data from such a GRI method. That is, there are neither standard experimental procedures for interpreting gas pulse-decay data in crushed rock samples nor detailed mathematical solutions available for data processing in the literature (Kim et al., 2015; Peng and Loucks, 2016; Profice et al., 2012). In this work, we achieve to: (1) develop mathematical solutions to interpret gas pulse-decay data in crushed rock samples without published algorithm available as this method shares different constitutive phenomena to the traditional pulse-decay method for core plug samples in Cartesian coordinates; and (2) present associated experimental methodology to measure permeability, reliably and reproducibly, in tight and ultra-tight granular media.

We first derive the constitutive equations for gas transport in granular (unconsolidated or crushed rock) samples. Specifically, we develop three mathematical solutions which cover different experimental situations and sample properties. As each solution shows its own pros and cons, we then in detail present the error analyses for the derived exact and approximate

115 solutions and discuss their applicable requirements and parameter
116 recommendation for practical usages. This work aims to fill the knowledge
117 gap of the granular rock (matrix) permeability measurement and follow-on
118 literature by establishing an integrated methodology for reproducible
119 measurements of nD-level permeability in tight rock for emerging energy and
120 resources subsurface studies.

121 **2. Mathematical solutions for gas permeability of granular samples**

122 For a compressible fluid under unsteady-state conditions, flow in a porous
123 medium can be expressed by the mass conservation equation:

124 $$\frac{\partial p}{\partial t} + \nabla \cdot (\rho \overline{v}) = 0 \qquad (1A)$$

125 where p is the pressure, t is the time, ρ is the fluid density, and $\overline{v}$ is the
126 Darcy velocity. In continuity equations derived for gas flow in porous media,
127 permeability can be treated as a function of pressure through the ideal gas law.
128 Constitutive equations are commonly established for a small pressure
129 variation to avoid the non-linearity of gas (the liquid density to be a constant)
130 and to ensure that pressure would be the only unknown parameter (Haskett et
131 al., 1988). For spherical coordinates of fluid flow in porous media, assuming
132 flow along the radial direction of each spherical solid grain, Eq. (1A) becomes

133 $$\frac{\partial p}{\partial t}\phi = \frac{1}{c_t}\frac{k}{\mu r^2}\frac{\partial}{\partial r}\left(r^2 \frac{\partial p}{\partial r}\right) \qquad (1B)$$

The gas compressibility c_t is given by

$$c_t = \frac{1}{\rho}\frac{d\rho}{dp} = \frac{1}{p} - \frac{1}{z}\frac{dz}{dp} \quad (1C)$$

In Eqs. (1B) and (1C), ϕ and k are sample porosity and permeability, r is the migration distance of fluid, μ is the fluid viscosity, and z is the gas deviation (compressibility) factor and is constant.

To correct for the non-ideality of the probing gas, we treat gas density as a function of pressure and establish a relationship between the density and the permeability through a pseudo-pressure variable (given in the 1st part of Supplemental Information SI1). Detailed steps for deriving mathematical solutions for the GPT can be found in SI2, based on heat transfer studies (Carslaw and Jaeger, 1959). The Laplace transform is an efficient tool for solving gas transport in granular samples with low permeabilities, as applied in this study. Alternatively, other approaches, such as the Fourier analysis, Sturm-Liouville method, or Volterra integral equation of the second form may be used (Carslaw and Jaeger, 1959; Haggerty and Gorelick, 1995; Ruthven, 1984).

We applied dimensional variables to derive the constitutive equation given in Eq. (S10) for which the initial and boundary conditions are

$$\frac{\partial^2 U_s}{\partial \xi^2} + s^2 U_s = 0\Big|_{U_s=0,\xi=0} \quad (2A)$$

$$\alpha^2(U_s - 1) = \frac{3}{K_c}\left(\frac{\partial U_s}{\partial \xi} - \frac{U_s}{\xi}\right)\Big|_{\xi=1} \quad (2B)$$

where U_s and ξ represent the dimensionless values of gas density and sample scale, and s is the transformed Heaviside operator. α in Eq. (2B) is determined by solving Eq. (S30) for its root. K_c in Eq. (2B) is a critical parameter that represents the volumetric ratio of the total void volume of the sample cell to the pore volume of the porous samples. It is similar to the storage capacity, controlling the acceptable measurement range of permeability and decay time, in the pulse-decay method proposed by Brace et al. (1968).

The fractional gas transfer for the internal (limited K_c value) and external (infinite K_c value) gas transfer of sample is given by

$$F_f = 1 - 6\sum_{n=1}^{\infty} \frac{K_c(1+K_c)e^{-\alpha_n{}^2\tau}}{9(K_c+1)+\alpha_n{}^2 K_c{}^2} \quad (2C)$$

$$F_s = 1 - \frac{6}{\pi^2}\sum_{n=1}^{\infty} \frac{e^{-(n\pi)^2\tau}}{n^2} \quad (2D)$$

where F_f and F_s represent the uptake rate of gas outside and inside the sample separately as a dimensionless parameter, and τ is the Fourier number of dimensionless time. Three approximate solutions of the transport

coefficient based on Eqs. (2C) and (2D) for various conditions are presented below.

The late-time solution to Eq. (2C) for a limited K_c value (called LLT hereafter) is

$$k = \frac{{R_a}^2 \mu c_t \phi_f s_1}{{\alpha_1}^2} \quad (3A)$$

The late-time solution to Eq. (2D) when K_c tends to infinity (ILT hereafter) is

$$k = \frac{{R_a}^2 \mu c_t \phi_f s_2}{\pi^2} \quad (3B)$$

The early-time solution to Eq. (2D) when K_c approaches infinity (IET hereafter) is

$$k = \frac{\pi {R_a}^2 \mu c_t \phi_f s_3}{36} \quad (3C)$$

In Eq. (3), R_a is the particle diameter of a sample, and s_1, s_2, and s_3 are the three exponents that may be determined from the slopes of data on double logarithmic plots. Table 1 summarizes Eqs. (3A) to (3C) and conditions under which such approximate solutions would be valid.

Table 1. Solutions schematic with difference K_c and τ values

Parameter	Symbol	Remarks		
Volume fraction[§]	K_c	Limited value for $K_c < 10$	Infinity value for $K_c > 10$	
Exact. Density fraction[£]	F	F_f	F_s	
Approx. Solution of Density fraction[*]	Eqs. (3A-3B)	Eq. (3A) (LLT)	Eq. (3C) (IET)	Eq. (3B)) (ILT)
Available Dimensionless time for Approx. solution	τ	Late-time solution $\tau > 0.024$	Early-time solution $\tau < 0.024$	Late-time solution $\tau > 0.024$

[§] It defines as the volumetric ratio of the total void volume of the sample cell to the pore volume of the porous samples, the classification between the limited and infinity value is proposed as 50 with the following analyses.

[£] The original constitutive equation for different K_c value.
[*] Eqs. (3A-3C) are three approximate solutions of density faction function F.

Based on diffusion phenomenology, Cui et al. (2009) presented two mathematical solutions similar to our Eqs. (3A) and (3C). In the work of Cui et al. (2009), however, one of late-time solution is missing, and error analyses are not provided. Besides, the lack of detailed analyses of τ and K_c in the constitutive equations will likely deter the practical application of Eq. (3B), which is able to cover an experimental condition of small sample mass with a greater τ (further analyzed in Section 3). Furthermore, the early-time and late-time solution criteria are not analyzed, and the pioneering work of Cui et al. (2009) does not comprehensively assess practical applications of their two solutions in real cases, which is addressed in this study. Hereafter, we refer to the developed mathematical and experimental, gas-permeability-measurement approach holistically as gas permeability technique (GPT).

3. Practical usages of algorithms for the GPT

As aforementioned, mathematical solutions given in Eqs. (3A) and (3B) were deduced based on different values of K_c and τ as shown in the SI2. This means each solution holds only under specific experimental conditions, which are mostly determined by the permeability, porosity, and mass of samples, as well as gas pressure and void volume of the sample cell. In this section, the influence of parameters K_c and τ on the solution of constitutive

equation is analyzed and a specific value of dimensionless time (τ = 0.024) is proposed as the criterion required to detect the early-time regime from the late-time one for the first time in the literature. We also demonstrate that the early-time solution of Eq. (3C), which has been less considered for practical applications in previous studies, is also suitable and unique under common situations. Besides, the error of the approximate solution compared to the exact solution and their capabilities are discussed, as it helps to select an appropriate mathematical solution at small τ values. Moreover, we showcase the unique applicability and feasibility of the new solution of Eq. (3B).

3.1 Sensitivity analyses of the K_c value for data quality control

To apply the GPT method, appropriately selecting the parameter K_c in Eqs. (3A)-(3C) is crucial, as it is a critical value for data quality control. The dimensionless density outside the sample, U_f, is related to K_c via Eq. (S33) in the SI2. One may simplify Eq. (S33) by replacing the series term with some finite positive value and set

$$U_f - \frac{K_c}{1+K_c} > 0 \qquad (1G)$$

We define $K_f = K_c/(1 + K_c)$ to interpret the density variance of the system as K_f is closely related to the dimensionless density outside the sample, U_f.

Eq. (1G) shows the relationship between the U_f and K_c (Fig. 1). For

223 $K_c > 0$, K_f falls between 0 and 1. The greater the K_f value is, the insensitive
224 to density changes the system would be. For K_c equal to 50, K_f would no
225 longer be sensitive to K_c variations as it has already approached 98% of the
226 dimensionless density. This means that the U_f value needs to be greater than
227 0.98, and this leaves only 2% of the fractional value of U_f available for
228 capturing gas density change. When K_c is 100, the left fractional value of U_f
229 would be 1%. This would limit the amount of data available (the linear range
230 in Fig. S1) for the permeability calculation, which would complicate the data
231 processing. Thus, for the GPT experiments, a small value of K_c (less than 10)
232 is recommended, as K_f nearly reaches its plateau beyond K_c = 10 (Fig. 1).
233 When K_c is 10, the left fractional value of U_f is only as low as 9%.

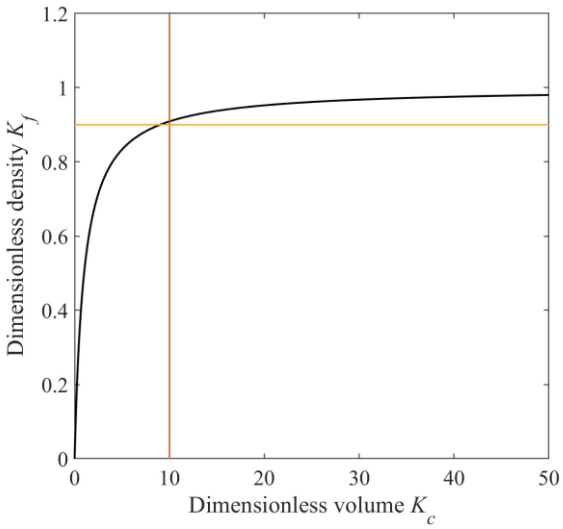

234

Fig. 1. Dimensionless density, K_f, as a function of dimensionless volume K_c. Major variations in K_f occur for K_c < 10 indicating longer gas transmission duration with more pressure-decay data available for permeability derivation.

3.2 Recommendation for solution selection

The following three aspects need to be considered before selecting the appropriate solution for permeability calculation: 1) early- or late-time solutions; 2) error between the approximate and exact solutions; and 3) the convenience and applicability of solutions suitable for different experiments. We will first discuss the selection criteria for early- or late-time solutions.

Fig. 2(a) shows the exact solution of F_s with their two approximate early- and late-time solution (Table 1). Two exact solutions of F_f where K_c equals to 10 or 50 are also demonstrated in Fig. 2(a). Fig. 2(b) depicts the exact solution from F_f for different K_c values from 1 to 100 and their corresponding approximate solution for Eq. (3A). The intersection point of the solution Eq. (3B) and Eq. (3C), namely τ = 0.024 in Fig. 2(a), is used for distinguishing early- and late-time solutions.

Two notable observations can be drawn from Fig. 2(b). Firstly, the approximate solution Eq. (3A) would only be applicable at late times when τ is longer than 0.024. For $\tau < 0.024$, regardless of the K_c value, Eq. (3C)

would be more precise than Eqs. (3A) and (3B) and return results close to the exact solution for both F_f and F_s. Secondly, results of Eqs. (3A) and (3B) presented in Fig. 2(a) are similar; there difference is very small especially for $K_c > 10$. Due to the fact that core samples from deep wells are relatively short in length and their void volume is small (ultra-low porosity and permeability such as in mudrocks with $k \leq 0.1$ nD), in practice, a solution for $10< K_c <100$ is the most common outcome, even if the sample cell is loaded as full as possible. Under such circumstances, the newly derived solution, Eq. (3B), becomes practical and convenient: 1) if the K_c and dimensionless time τ have not been evaluated precisely before the GPT experiment, this solution may fit most experimental situations; 2) this solution is suitable for calculation as it does not need the solution from the transcendental equation of Eq. (S30) because the denominator of α has been replaced by π. The data quality control is discussed in Section 4.1.

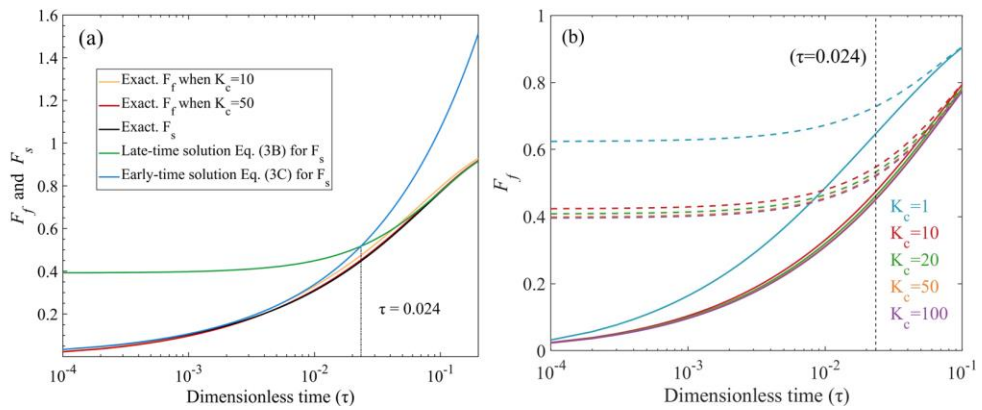

Fig. 2. Three GPT solutions with different values of τ, K_c; the dashed lines are approximate solutions without a series expansion in Fig. (2b) for F_f. Figure modified from Cui et al. (2009).

3.3 Applicability of the early-time solution

A small K_c value can guarantee a sufficient time for gas transfer in samples and provide enough linear data for fitting purposes. We note that the selection of the limited K_c solution of F_f, and the infinity K_c solution F_s is controlled by K_c. However, before the selection of K_c, the dimensionless time is the basic parameter to be estimated as a priori before the early- or late-time solutions are selected.

For pulse-decay methods, the early-time solution has the advantage of capturing the anisotropic information contained in reservoir rocks (Jia et al., 2019; Kamath, 1992). However, it suffers from the shortcoming of uncertainty in data for initial several seconds, which as a result is not recommended for data processing (Brace et al., 1968; Cui et al., 2009). This is due to: (1) the Joule-Thompson effect, which causes a decrease in gas temperature from the expansion; (2) kinetic energy loss during adiabatic expansion; and (3) collision between molecules and the container wall. These uncertainties normally occur in the first 10-30 sec, shown in our experiments as a fluctuating period called

"Early Stage".

However, the "Early Stage" present in pulse-decay experiments does not mean that the early-time solution is not applicable. We demonstrate the relationship between time and dimensionless time in Fig. 3 that a short dimensionless time may correspond to a long testing period of hundred to thousand seconds in experiments. This is particularly noticeable for the ultra-low permeability samples with $k \leq 0.1$ nD and small dimensionless times $\tau < 0.024$. This situation would only be applicable to early-time solution, but with data available beyond the "Early Stage" and provide available data in a long time (hundreds to thousands of seconds). For example, the early-time solution would fit ultra-low permeability samples in 600s for 0.1 nD, and at least 1000s for 0.01 nD shown in Fig. 3 in the region below the dark line. Then, using Eq. (3C), the derived permeability would be closer to its exact solution in the earlier testing time (but still after the "Early Stage"). The mudrock samples that we tested, with results presented in Section 5.3, exhibit low permeabilities, approximately on the order of 0.1 nD.

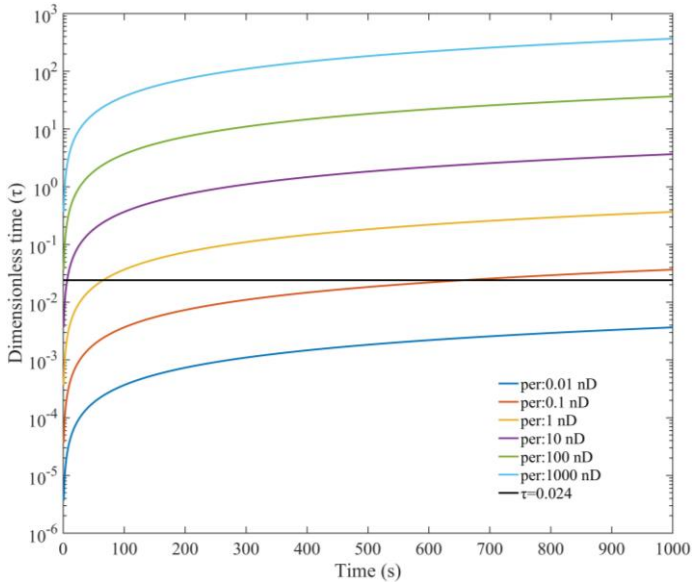

Fig. 3 Dimensionless time τ versus actual times for different permeability values trough Eq. (S14) using He gas, sample porosity of 5%, and sample diameter of 2 mm.

3.4 Error analyses between exact and approximate solutions

It is unpractical to use the exact solutions with their series part to do the permeability calculation; thus, only the approximate solutions are used and the error difference between the exact and approximate solutions is discussed here. The original mathematical solutions, Eqs. (S39) and (S49), are based on series expansion. For dimensionless densities F_f and F_s in Eqs. (S39) and (S49), their series expansion terms should converge. However, the rate of convergence is closely related to the value of τ. For example, from Eq. (S30), when $\tau \geq 1$, the exponent parts of U_s and U_f are at least $(2n+1)\pi^2$.

318 Therefore, the entire series expansion term can be omitted without being
319 influenced by K_c. In practical applications, the solutions given in Eqs. (3A)-
320 (3C) are approximates without series expansion. In this study, we provide the
321 diagrams of change in errors with dimensionless time in the presence of
322 adsorption (Fig. 4).

323 For F_f, the error differences between the exact and approximate solutions
324 are 3.5% and 0.37% for τ = 0.05 and 0.1 when K_c = 10, respectively. When
325 $\tau \leq$ 0.024, the error would be greater than 14.7%. Fig. 2(b) shows that F_f
326 can be approximated as F_s when K_c is greater than 10; the error difference
327 between F_f and F_s is quite small at this K_c value (for K_c = 10, 6.6% is the
328 maximum error when τ = 0.01; 4.4% when τ = 0.05; and 2.9% when τ = 0.1)
329 as shown in Fig. 4.

330 For F_s, the error difference is roughly the same as F_f and equal to 3.6%
331 for τ = 0.05 and 0.38% for τ = 0.1. This verifies that newly derived Eq. (3B)
332 is equivalent to Eq. (3A) when K_c is greater than 10. As for the evaluation
333 of Eq. (3C), the error difference with the exact solution will increase with
334 dimensionless time (5.1% for τ = 0.003, 9.7% for τ = 0.01, and 16% for τ =
335 0.024).

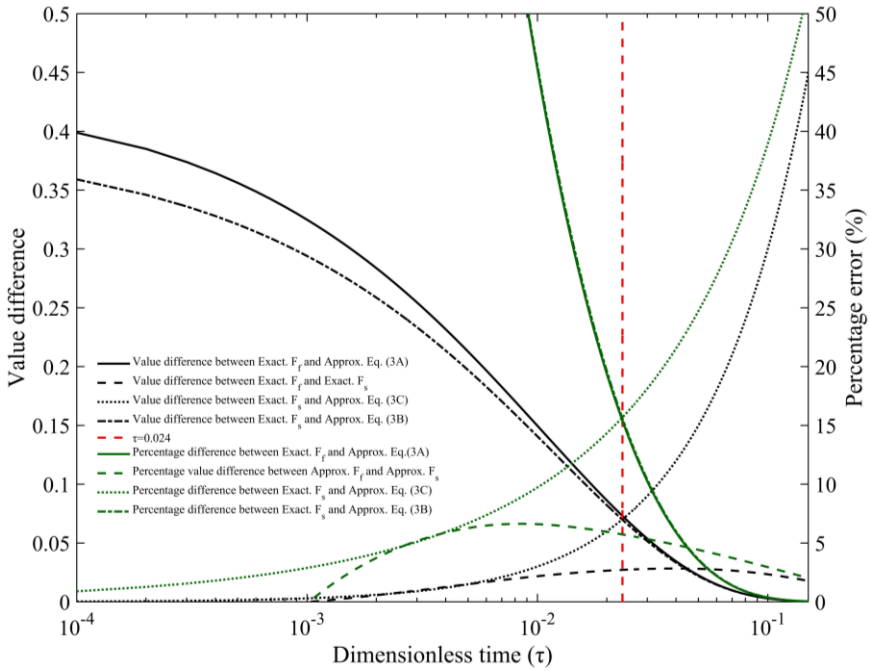

Fig. 4. Error analyses of F_f and F_s for their exact and approximate solutions

4. Influence of kinetic energy on gas transport behavior

4.1 Flow state of gas in granular samples

In the following, we apply the approximate solutions, Eqs. (3A-3C), to some detailed experimental data and determine permeability in several mudrock samples practically compatible with sample size, gases, and molecular dynamics analyses.

During the GPT, with the boundary conditions described in SI2, the pressure variation is captured after gas starts to permeate into the sample from the edge, and the model does not take into account the gas transport between particles or into any micro-fractures, if available. Thus, the transport that conforms to

348 the "unipore" model and occurs after the "Early Stage" (defined in Section 3.3)
349 or during the "Penetration Zone" (the area between the two vertical lines in
350 Fig. 5), should be used to determine the slope. Fig. S2 shows how to obtain
351 the permeability result using the applicable mathematical solutions (Eqs. 3A-
352 C). Fig. 5 shows the pressure variance with time during the experiment using
353 sample size from 0.34 mm to 5.18 mm for sample X-1 and sample X-2. From
354 Fig. 5, the time needed to reach pressure equilibrium after the initial
355 fluctuation stage is 20-100 sec, and the “Penetration Zone” decreases with
356 decreasing grain size over this time period.

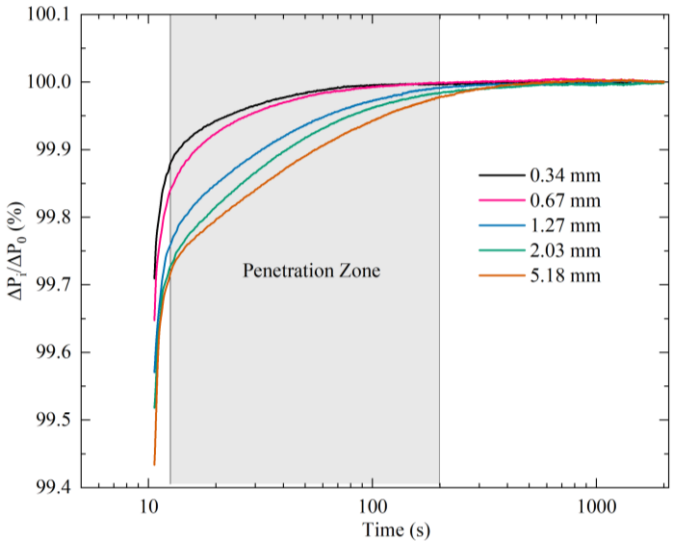

357

358 Fig. 5. Fitting region (the "Penetration Zone" in the shadowed area) for mudrock
359 sample X-1 with different granular sizes; the penetration zone illustrating the
360 pressure gradient mainly happens at 20 to 200 sec for this sample.
361

In fact, the "Penetration Zone", as an empirical period, is evaluated by the pressure change over a unit of time before gas is completely transported into the inner central part of the sample to reach the final pressure. Owing to the sample size limitation, a decreasing pressure could cause multiple flow states (based on the Knudsen number) to exist in the experiment. The pressure during the GPT experiment varies between 50 and 200 psi (0.345 MPa to 1.38 MPa). Fig. 6 shows the Knudsen number calculated from different pressure conditions and pore diameters together with their potential flow state. Based on Fig. 6, the flow state of gas in the GPT experiments is mainly dominated by Fickian and transition diffusion. Essentially, the flow state change with pressure should be strictly evaluated through the Knudsen number in Fig. 6 to guarantee that the data in the "Penetration Zone" are always fitted with the GPT's constitutive equation for laminar or diffusive states. This helps obtain a linear trend for $ln(1 - F_f)$ or ${F_s}^2$ versus time for low-permeability media. Experimentally, data from 30 to several 100 seconds are recommended for tight rocks like shales within the GPT methodology.

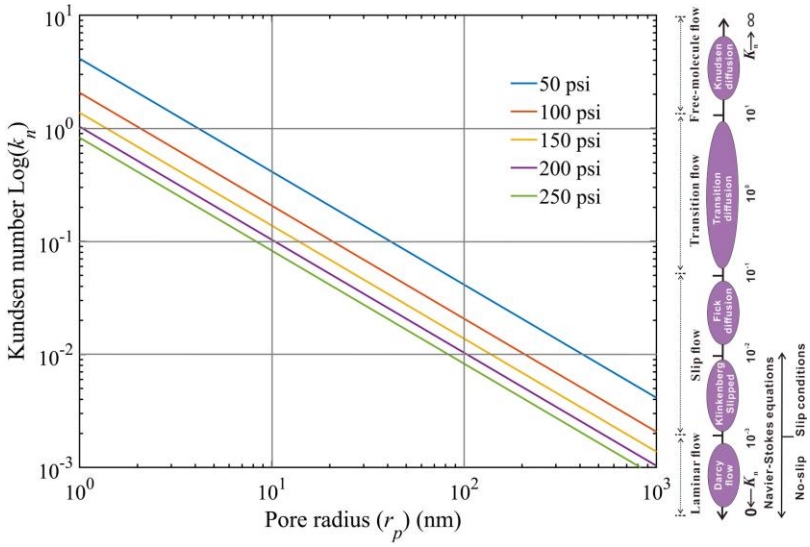

Fig. 6. Flow state of gas under diffferent testing pressures; modified from Chen & Pfender (1983) and Roy et al. (2003) (Chen and Pfender, 1983; Roy et al., 2003).

In the GPT approach, as mentioned earlier, Eq. (S33) holds for small K_c values (e.g., < 10) so that the approximately equivalent void volume in the sample cell and sample pore volume would allow for sufficient pressure drop. It also gives time and allows the probing gas to expand into the matrix pores to have a valid "Penetration Zone" and to determine the permeability. Greater values of K_c would prevent the gas flow from entering into a slippage state as the pressure difference would increase with increasing K_c. However, large pressure changes would result in a turbulent flow (Fig. 6), which would cause the flow state of gas to be no longer valid for the constitutive equation of the GPT. Overall, the GPT solutions would be applicable to the gas permeability

measurement, based on the diffusion-like process, from laminar flow to Fickian diffusion, after the correction of the slippage effect.

4.2 Pressure decay behavior of four different probing gases

We used three inert gases, including He, N_2, and Ar, and one sorptive gas i.e., CO_2 (Busch et al., 2008), to compare the pressure drop behavior for sample size with an average granular diameter of 0.675 mm. Results for the mudrock sample X-2 are presented in Fig. 7. Among the three inert gases, helium and argon required the shortest and longest time to reach pressure equilibrium (i.e., He<N_2<Ar). In terms of pressure drop, argon exhibited the most significant decrease. In a constant-temperature system, the speed (or rate) at which gas molecules move is inversely proportional to the square root of their molar masses. Hence, it is reasonable that helium (with the smallest kinetic diameter of 0.21 nm) has the shortest equilibrium time. However, the pressure drop is more critical than the time needed to reach equilibrium for the GPT, as the equilibrium time does not differ much (basically within 10 seconds for a given sample weight, except for the adsorptive CO_2). Argon may provide a wider range of valid Penetration Zones in a short time scale for its longest decay time except for adsorbed gas of CO_2; a choice of inert and economical gas is suggested for the GPT experiments.

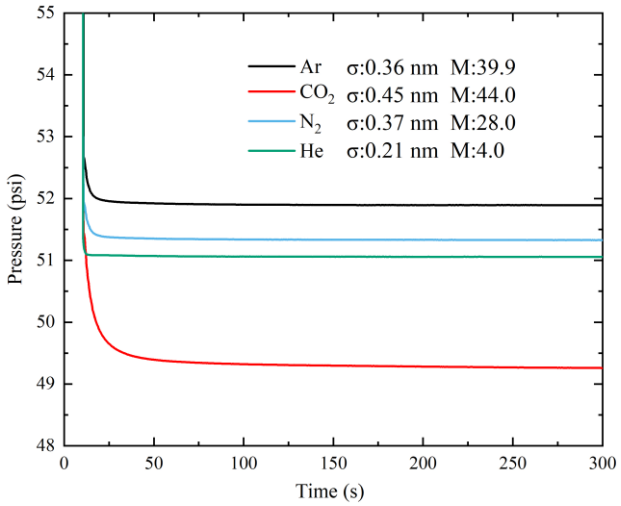

411

412 Fig. 7. Measured pressure decay curves from mudrock Sample X-2 for gases of
413 different molecular diameters σ and molecular weights M (g/mol).

414

415 Fig. 7 shows that the pressure decay curve of the adsorptive gas CO_2 is
416 different from those of the inert gases used in this study. CO_2 has a slow
417 equilibrium process due to its large molar mass, and the greatest pressure drop
418 among the four gases due to its adsorption effect. This additional flux needs to
419 be taken into account to obtain an accurate transport coefficient. Accordingly,
420 multiple studies including laboratory experiments (Pini, 2014) and long-term
421 field observations (Haszeldine et al., 2006; Lu et al., 2009) were carried out to
422 assess the sealing efficiency of mudrocks for CO_2 storage. In fact, the GPT
423 can supply a quick and effective way to identify the adsorption behavior of
424 different mudrocks for both laminar-flow and diffusion states.

425 **4.3 Pressure decay behavior for different granular sizes**

426 We compared the pressure drop behavior of gas in the mudrock Sample X-
427 1 with different granular sizes (averaged from 0.34 mm to 5.18 mm) using the
428 same sample weight and K_c. Results based on the experimental data shown in
429 Fig. 8 indicate that a larger-sized sample would provide more data to be
430 analyzed for determining the permeability. This is because the larger the
431 granular size, and (1) the larger the pressure drop, (2) the longer the decay time
432 as Fig. 8 demonstrates. This is consistent with the simulated results reported
433 by Profice et al. (2012).

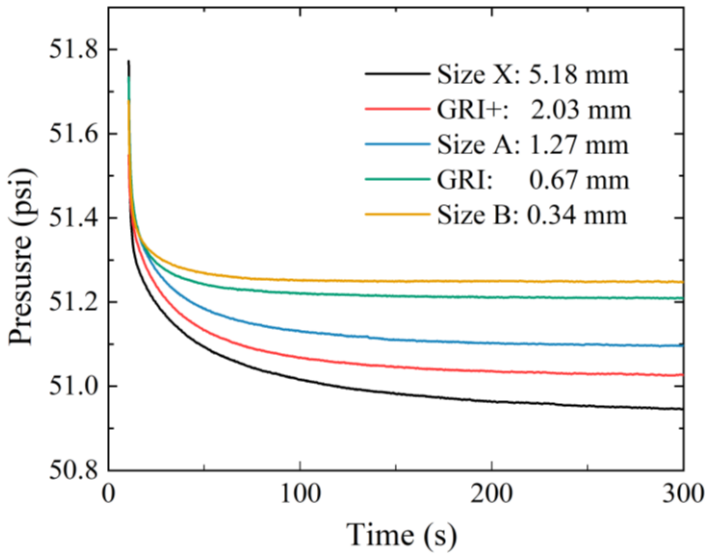

434

435 Fig. 8. Pressure decay curves measured by helium on sample X-1 with five different
436 granular sizes. The intra-granular porosity was 5.8% independently measured by
437 mercury intrusion porosimetry.

438

439 Table 2. Permeability results from the methods of GPT and SMP-200 for X-1.

Granular size (mm)	SMP-200 (nD) [§]	GPT test 1 (nD)[£]	GPT test 2 (nD)[£]	Average value (nD)[£]	Fitting duration (s)	Unselected Solution (nD)*	Dimensionless time	Particle density (g/cm^3)
5.18	-	1.17	1.17	1.17(ILT)	50-100	239(IET) 1.31(LLT)	0.023-0.027	2.631
2.03	14.2	0.45	0.41	0.43(LLT)	50-100	11.1(IET) 0.36(ILT)	0.026-0.028	2.626
1.27	-	0.10	0.10	0.10(ILT)	30-60	20.5(IET) 0.09(ILT)	CR*	2.673
0.67	0.65	0.08	0.04	0.06(LLT)	30-60	1570(IET) 0.03(ILT)	CR*	2.658
0.34	-	0.02	-	0.02(IET)	30-60	0.00076(LLT) 0.00068(BLT)	CR*	2.643

[§] The results are from the SMP-200 using the GRI default method.

[£] The results are from the GPT method we proposed.

* CR means the conflict results that the verified dimensionless time does not confirm the early- or late-time solutions using the solved permeability. For example, the verified dimensionless time would be > 0.024 using the early-time solution solved result and vice versa.

* represents the result which failed for the criteria of dimensionless time

440 As reported in Table 2, the permeability values measured by the GPT
441 method are one or two orders of magnitude greater than those measured by the
442 SMP-200 instrument. The built-in functions of SMP-200 can only be used for
443 two default granular sizes (500-841 μm for GRI and 1.70-2.38 mm for what
444 we call GRI+) to manually curve-fit the pressure decay data and determine the
445 permeability. The GRI method built in the SMP-200 only suggests the fitting
446 procedure for data processing without publicly available details of underlying
447 mathematics. The intra-granular permeabilities of mudrocks sample X-1 vary
448 from 0.02 to 1.17 nD for five different granular sizes using the GPT. With the
449 same pressure decay data selected from 30 to 200 sec, the permeability results
450 for GRI and GRI+ sample sizes from the SMP-200 fitting are 0.65 and 14.2
451 nD, as compared to 0.06 and 0.43 nD determined by the GPT using the same

mean granular size. Our results are consistent with those reported by Peng & Loucks (2016) who found two to three orders of magnitude differences between the GPT and SMP-200 methods (Peng and Loucks, 2016).

There exist several issues associated with granular samples with diameters smaller than on average 1.27 mm. First, the testing duration is short, and second, there would not be sufficient pressure variation analyzed in Fig. 8. Both may cause significant uncertainties in the permeability calculation and, therefore, make samples with diameters smaller than 1.27 mm unfavorable for the GPT method, particularly extra-tight (sub-nD levels) samples, as there is almost no laminar or diffusion flow state to be captured. The greater pressure drop for larger-sized granular samples would result in greater pressure variation and wider data region compared to smaller granular sizes (see Figs. 6 and 9). Although samples of large granular sizes may potentially contain micro-fractures, which complicate the determination of true matrix permeability (Heller et al., 2014), the versatile GPT method can still provide size-dependent permeabilities for a wide range of samples (e.g., from sub-mm to 10 cm diameter full-size cores) (Ghanbarian, 2022a, b). Besides, the surface roughness of large grains may also complicate the determination of permeability, which need to pay attention to (Devegowda, 2015; Rasmuson, 1985; Ruthven and Loughlin, 1971). Overall, our results demonstrated that

sample diameters larger 2 mm are recommended for the GPT to determine the nD permeability of tight mudrocks, while smaller sample sizes may produce uncertain results.

4.4 Practical recommendations for the holistic GPT

Here, we evaluate the potential approximate solution for tight rock samples using frequently applied experimental settings by considering the critical parameters, such as sample mass, porosity, and estimated permeability (as compiled in Fig. 9 showing the dimensionless time versus porosity). Based on the results presented in Figs. 3 and 6, only $t < 200$s is dominant and critical for the analyses of dimensionless time and penetration zone. Thus, we take 200s and use helium to calculate the dimensionless time. Another critical parameter to assure enough decay data is the sample diameter greater than 2 mm. Thus, we only show the dimensionless time versus porosity for sample diameter greater than the criteria of 2 mm.

Fig. 9 demonstrates that the sample permeability has dominant control on the early- or late-solution selection, and we decipher a concise criterial for three solutions selection. We classify the dimensionless time versus porosity relationship into three cases. Firstly, among the curves shown in Fig. 9, only that corresponding to $k = 0.1$ nD and sample diameter of 2 mm stays below the dashed line representing $\tau = 0.024$. Therefore, the early time solution is

492 appropriate for tight samples with permeabilities less than 0.1 nD (as shown
493 in the analyses of Section 4.3, which also conforms to the situation of the
494 molecular sieve sample that we tested in SI3). Secondly, for permeabilities
495 greater than 10 nD (the curve is above the line of $\tau = 0.024$), the new derived
496 late-time solution, Eq. (3B), is recommended as it is more convenient for
497 mathematical calculation without the consideration of transcendental
498 functions. The reason is that the sample cell can be filled as much as possible
499 (~90% of the volume) with samples and solid objects. However, as the tight
500 rock hardly presents a large value of porosity, the small K_c value is difficult
501 to be achieved with an inconsequential influence between Eq. (3B) and Eq.
502 (3A). Lastly, in the case of permeability around 1 nD, the value of porosity
503 would be critical in the selection of the early- or late-time solutions, as shown
504 in Fig. 9.

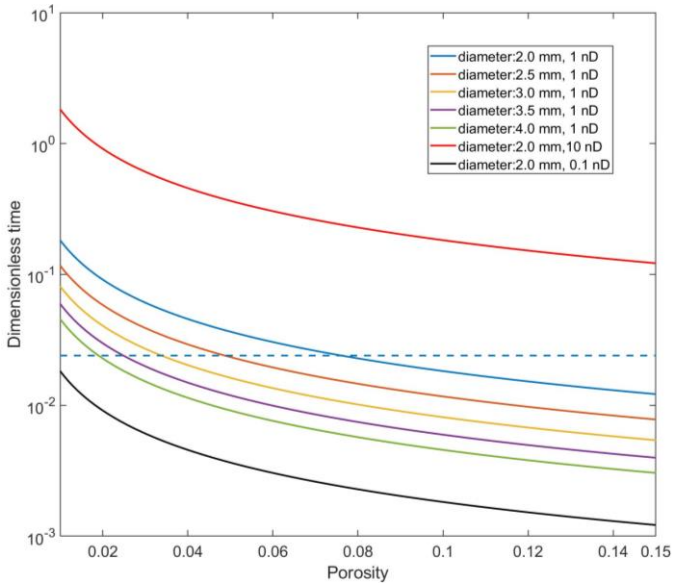

Fig. 9. Holistic GPT to explore the appropriate solution based on diameter, permeability, and porosity of samples. The legend shows the diameter of granular sample and permeability, along with a dashed line for dimensionless time of 0.024, while regions above and below this value fit for the late- and early-time solutions, respectively.

5. Conclusions

In the present work, we solved fluid flow state equation in granular porous media and provided three exact mathematical solutions along with their approximate ones for practical applications of low permeability measurements. The mathematical solutions for the transport coefficient in the GPT were derived for a spherical coordinate system, applicable from laminar flow to slippage-corrected Fickian diffusion. Of the three derived solutions, one is valid during early times when the gas storage capacity K_c approaches infinity,

519 while the other two are late-time solutions to be valid when K_c is either small
520 or tends towards infinity. We evaluated the derived solutions for a systematic
521 measurement of extra-low permeabilities in granular media and crushed rocks
522 using experimental methodologies with the data processing procedures. We
523 determined the error for each solution by comparing with the exact solutions
524 presented in the SI. The applicable conditions for such solutions of the GPT
525 were investigated, and we provided the selection strategies for three
526 approximate solutions based the range of sample permeability. In addition, a
527 detailed utilization of GTP was given to build up the confidence in the GPT
528 method through the molecular sieve sample, as it enables a rapid permeability
529 test for ultra-tight rock samples in just tens to hundreds of seconds, with good
530 repeatability.

531 **Data availability.** This work did not use any data from previously published
532 sources, and our experimental data & processing codes of MATLAB are
533 available at https://doi.org/10.18738/T8/YZJS7Y, managed by Mavs
534 Dataverse of the University of Texas at Arlington.

535 **Supplement.** An early-version preprint of this work appears as DOI:
536 10.1002/essoar.10506690.2 (Zhang et al., 2021).

537 **Author contributions**. TZ and QHH planned and designed the research,
538 performed the analyses, and wrote the paper with contributions from all co-
539 authors. BG, DK, and ZM participated in the research and edited the paper.

540 **Competing interest.** We declare that we do not have any commercial or

associative interest that represents a conflict of interest in connection with the work submitted.

Acknowledgments. Financial assistance for this work was provided by the National Natural Science Foundation of China (41830431; 41821002), Shandong Provincial Major Type Grant for Research and Development from the Department of Science & Technology of Shandong Province (2020ZLYS08), Maverick Science Graduate Research Fellowship for 2022-2023, the AAPG and the West Texas Geological Foundation Adams Scholarships, and Kansas State University through faculty start-up funds to BG. We extend our deepest appreciation to handling editor Monica Riva for her diligent assistance, and to the two anonymous referees for their insightful comments on this paper.

Nomenclature

B_{ij} Correction parameter for viscosity, constant

c_t Fluid compressibility, Pa^{-1}

F_f Uptake rate of gas outside the sample, dimensionless

F_s Uptake rate in the sample, dimensionless

f_1 Intercept of Eq. (S40), constant

K_a Apparent transport coefficient defined as Eq. (S9), m^2/s

K_c Ratio of gas storage capacity of the total void volume of the system to the pore (including adsorptive and non-adsorptive transport) volume of the sample, fraction

K_f Initial density state of the system, fraction

k Permeability, m^2

k_s Permeability defined as Eq. (S8), $m^2/(pa{\cdot}s)$

L Coefficient, unit for certain physical transport phenomenon

M Molar mass, kg/kmol

M_m Molar mass of the mixed gas, kg/kmol

$M_{i,j}$ Molar mass for gas i or j, kg/kmol

M_s Total mass of sample, kg

N Particle number, constant

p Pressure, Pa

p_{cm} Virtual critical pressure of mixed gas, Pa

p_p Pseudo-pressure from Eq. (S1), Pa/s

R_a Particle diameter of sample, m

R Universal gas constant, 8.314 J/(mol·K)

r Diameter of sample, m

s_1 Slope of Eq. (S40), constant

580 s_2 Slope of function $Ln(1-F_s)$, constant

581 s_3 Slope of function ${F_s}^2$, constant

582 T Temperature, K

583 T_{cm} Virtual critical temperature for mixed gas, K

584 t Time, s

585 U_f Dimensionless density of gas outside the sample, dimensionless

586 U_s Dimensionless density in grain, dimensionless

587 U_∞ Maximum density defined as Eq. (S37), dimensionless

588 V_1 Cell volume in upstream of pulse-decay method, m^3

589 V_2 Cell volume in downstream of pulse-decay method, m^3

590 V_b Bulk volume of sample, m^3

591 V_c Total system void volume except for sample bulk volume, m^3

592 $\overline{v}$ Dacian velocity in pore volume of porous media, m/s

593 X Pressure force, Pa

594 $y_{i,j}$ Molar fraction for gas i or j, fraction

595 z Gas deviation (compressibility) factor, constant

596 **Greek Letters:**

597 α_n The nth root of Eq. (S30), constant

598 μ Dynamic viscosity, pa·s or $N{\cdot}s/m^2$

599 $\mu_{i,j}$ Dynamic viscosity for gas i or j, pa·s or $N{\cdot}s/m^2$

600 μ_{mix} Dynamic viscosity of mixture gas, pa s or N s/m^2

601 μ_p Correction term for the viscosity with pressure, pa s or N s/m^2

602 ξ Dimensionless radius of sample, dimensionless

603 ρ Density of fluid, kg/m^3

604 ρ_0 Average gas density on the periphery of sample, kg/m^3

ρ_1 Gas density in reference cell, kg/m^3

ρ_2 Gas density in sample cell, kg/m^3

ρ_b Average bulk density for each particle, kg/m^3

ρ_f Density of gas changing with time outside sample, kg·m^{-3}·s^{-1}

$\rho_{f\infty}$ Maximum value of ρ_f defined as Eq. (S38), kg·m^{-3}·s^{-1}

ρ_p Pseudo-density from Eq. (S1), kg·m^{-3}·s^{-1}

ρ_s Density of gas changing with time in sample, kg·m^{-3}·s^{-1}

ρ_{ps} Pseudo-density of gas changing with time in sample, kg·m^{-3}·s^{-1}

ρ_{pf} Pseudo-density of gas changing with time outside sample, kg·m^{-3}·s^{-1}

ρ_{p2} Initial pseudo-density of gas in sample, kg·m^{-3}·s^{-1}

ρ_{p0} Average pseudo-density of gas on sample periphery, kg·m^{-3}·s^{-1}

ρ_{rm} Relative density to the mixed gas, kg·m^{-3}·s^{-1}

ρ_{sav} Average value ofρ_{sr}defined as Eq. (S47), kg·m^{-3}·s^{-1}

ρ_{sr} Average value of pseudo-density of sample changing with diameter, kg·m^{-3}·s^{-1}

$\rho_{s\infty}$ Maximum value of ρ_{sr} defined as Eq. (S46), kg·m^{-3}·s^{-1}

τ Dimensionless time, dimensionless

ϕ Sample porosity, fraction

ϕ_f Total porosity ($\phi_f = \phi_a + \phi_b$) occupied by both free and adsorptive fluids, fraction

References:

Abdassah, D., Ershaghi, I., 1986. Triple-porosity systems for representing naturally fractured reservoirs. Spe Formation Evaluation 1(02), 113-127.

Bibby, R., 1981. Mass transport of solutes in dual‐porosity media. Water Resour. Res. 17(4), 1075-1081.

Bock, H., Dehandschutter, B., Martin, C.D., Mazurek, M., De Haller, A., Skoczylas, F., Davy, C., 2010. Self-sealing of fractures in argillaceous formations in the context of geological disposal of radioactive waste.

Brace, W.F., Walsh, J.B., Frangos, W.T., 1968. Permeability of granite under high pressure. Journal of Geophysical Research 73(6), 2225-2236.

Busch, A., Alles, S., Gensterblum, Y., Prinz, D., Dewhurst, D.N., Raven, M.D., Stanjek, H., Krooss, B.M., 2008. Carbon dioxide storage potential of shales. Int. J. Greenh. Gas Control 2(3), 297-308.

Carslaw, H.S., Jaeger, J.C., 1959. Conduction of heat in solids.

Chen, X., Pfender, E., 1983. Effect of the Knudsen number on heat transfer to a particle immersed into a thermal plasma. Plasma Chem. Plasma Process. 3(1), 97-113.

Civan, F., Devegowda, D., Sigal, R.F., 2013. Critical evaluation and improvement of methods for determination of matrix permeability of shale, Society of Petroleum Engineers.

Cui, X., Bustin, A., Bustin, R.M., 2009. Measurements of gas permeability and diffusivity of tight reservoir rocks: different approaches and their applications. Geofluids 9(3), 208-223.

Devegowda, D., 2015. Comparison of shale permeability to gas determined by pressure-pulse transmission testing of core plugs and crushed samples, Unconventional Resources Technology Conference (URTEC).

Egermann, P., Lenormand, R., Longeron, D.G., Zarcone, C., 2005. A fast and direct method of permeability measurements on drill cuttings. Spe Reserv. Eval. Eng. 8(04), 269-275.

Fakher, S., Abdelaal, H., Elgahawy, Y., El-Tonbary, A., 2020. A Review of Long-Term Carbon Dioxide Storage in Shale Reservoirs, OnePetro.

Gensterblum, Y., Ghanizadeh, A., Cuss, R.J., Amann-Hildenbrand, A., Krooss, B.M., Clarkson, C.R., Harrington, J.F., Zoback, M.D., 2015. Gas transport and storage capacity in shale gas reservoirs – A review. Part A: Transport processes. Journal of Unconventional Oil and Gas Resources 12, 87-122.

Ghanbarian, B., 2022a. Estimating the scale dependence of permeability at pore and core scales: Incorporating effects of porosity and finite size. Adv. Water Resour. 161, 104123.

Ghanbarian, B., 2022b. Scale dependence of tortuosity and diffusion: Finite-size scaling analysis. J. Contam. Hydrol. 245, 103953.

671 Ghanbarian, B., Hunt, A.G., Daigle, H., 2016. Fluid flow in porous media with rough pore‐
672 solid interface. Water Resour. Res. 52(3), 2045-2058.
673 Guidry, K., Luffel, D., Curtis, J., 1996. Development of laboratory and petrophysical
674 techniques for evaluating shale reservoirs. Final technical report, October 1986-
675 September 1993, ResTech Houston, Inc., TX (United States).
676 Gutierrez, M., Øino, L.E., Nygaard, R., 2000. Stress-dependent permeability of a de-
677 mineralised fracture in shale. Mar. Pet. Geol. 17(8), 895-907.
678 Haggerty, R., Gorelick, S.M., 1995. Multiple‐rate mass transfer for modeling diffusion and
679 surface reactions in media with pore‐scale heterogeneity. Water Resour. Res. 31(10),
680 2383-2400.
681 Haskett, S.E., Narahara, G.M., Holditch, S.A., 1988. A method for simultaneous
682 determination of permeability and porosity in low-permeability cores. Spe Formation
683 Evaluation 3(03), 651-658.
684 Haszeldine, S., Lu, J., Wilkinson, M., Macleod, G., 2006. Long-timescale interaction of CO2
685 storage with reservoir and seal: Miller and Brae natural analogue fields North Sea.
686 Greenhouse Gas Control Technology 8.
687 Heller, R., Vermylen, J., Zoback, M., 2014. Experimental investigation of matrix permeability
688 of gas shalesExperimental Investigation of Matrix Permeability of Gas Shales. Aapg Bull.
689 98(5), 975-995.
690 Hu, Q., Ewing, R.P., Dultz, S., 2012. Low pore connectivity in natural rock. J. Contam. Hydrol.
691 133, 76-83.
692 Hu, Q., Ewing, R.P., Rowe, H.D., 2015. Low nanopore connectivity limits gas production in
693 Barnett formation. Journal of Geophysical Research: Solid Earth 120(12), 8073-8087.
694 Huenges, E., 2016., pp. 743-761, Elsevier.
695 Javadpour, F., 2009. Nanopores and apparent permeability of gas flow in mudrocks (shales
696 and siltstone). Journal of Canadian Petroleum Technology 48(08), 16-21.
697 Jia, B., Tsau, J., Barati, R., Zhang, F., 2019. Impact of Heterogeneity on the Transient Gas
698 Flow Process in Tight Rock. Energies 12(18), 3559.
699 Kamath, J., 1992. Evaluation of accuracy of estimating air permeability from mercury-
700 injection data. Spe Formation Evaluation 7(04), 304-310.
701 Khosrokhavar, R., 2016. Shale gas formations and their potential for carbon storage:
702 opportunities and outlook. Mechanisms for Co2 Sequestration in Geological Formations
703 and Enhanced Gas Recovery, 67-86.
704 Kim, C., Jang, H., Lee, J., 2015. Experimental investigation on the characteristics of gas
705 diffusion in shale gas reservoir using porosity and permeability of nanopore scale. J. Pet.
706 Sci. Eng. 133, 226-237.

Kim, J., Kwon, S., Sanchez, M., Cho, G., 2011. Geological storage of high level nuclear waste. Ksce J. Civ. Eng. 15(4), 721-737.

Liu, W., Li, Y., Yang, C., Daemen, J.J., Yang, Y., Zhang, G., 2015. Permeability characteristics of mudstone cap rock and interlayers in bedded salt formations and tightness assessment for underground gas storage caverns. Eng. Geol. 193, 212-223.

Lu, J., Wilkinson, M., Haszeldine, R.S., Fallick, A.E., 2009. Long-term performance of a mudrock seal in natural CO2 storage. Geology 37(1), 35-38.

Luffel, D.L., Hopkins, C.W., Schettler Jr, P.D., 1993. Matrix permeability measurement of gas productive shales, Society of Petroleum Engineers.

Neuzil, C.E., 1986. Groundwater flow in low ‐ permeability environments. Water Resour. Res. 22(8), 1163-1195.

Neuzil, C.E., 2013. Can shale safely host US nuclear waste? Eos, Transactions American Geophysical Union 94(30), 261-262.

Peng, S., Loucks, B., 2016. Permeability measurements in mudrocks using gas-expansion methods on plug and crushed-rock samples. Mar. Pet. Geol. 73, 299-310.

Pini, R., 2014. Assessing the adsorption properties of mudrocks for CO2 sequestration. Energy Procedia 63, 5556-5561.

Profice, S., Lasseux, D., Jannot, Y., Jebara, N., Hamon, G., 2012. Permeability, porosity and klinkenberg coefficien determination on crushed porous media. Petrophysics 53(06), 430-438.

Rasmuson, A., 1985. The effect of particles of variable size, shape and properties on the dynamics of fixed beds. Chem. Eng. Sci. 40(4), 621-629.

Roy, S., Raju, R., Chuang, H.F., Cruden, B.A., Meyyappan, M., 2003. Modeling gas flow through microchannels and nanopores. J. Appl. Phys. 93(8), 4870-4879.

Ruthven, D.M., 1984. Principles of adsorption and adsorption processes, John Wiley & Sons.

Ruthven, D.M., Loughlin, K.F., 1971. The effect of crystallite shape and size distribution on diffusion measurements in molecular sieves. Chem. Eng. Sci. 26(5), 577-584.

Tarkowski, R., 2019. Underground hydrogen storage: Characteristics and prospects. Renewable and Sustainable Energy Reviews 105, 86-94.

Wu, T., Zhang, D., Li, X., 2020. A radial differential pressure decay method with micro-plug samples for determining the apparent permeability of shale matrix. J. Nat. Gas Sci. Eng. 74, 103126.

Yang, M., Annable, M.D., Jawitz, J.W., 2015. Back diffusion from thin low permeability zones. Environ. Sci. Technol. 49(1), 415-422.

Zhang, J.J., Liu, H., Boudjatit, M., 2020. Matrix permeability measurement from fractured unconventional source-rock samples: Method and application. J. Contam. Hydrol.,

103663.

Zhang, T., Hu, Q., Chen, W., Gao, Y., Feng, X., Wang, G., 2021. Analyses of True-Triaxial Hydraulic Fracturing of Granite Samples for an Enhanced Geothermal System. Lithosphere 2021(Special 5).

Zhang, T., Zhou, W., Hu, Q., Xu, H., Zhao, J., Zhang, C., 2021. A pulse-decay method for low permeability analyses of granular porous media: Mathematical solutions and experimental methodologies.